

The host galaxies of $z = 7$ quasars: predictions from the BLUETIDES simulation

Madeline A. Marshall^{1,2}★, Yueying Ni³, Tiziana Di Matteo³★, J. Stuart B. Wyithe^{1,2}★
 Stephen Wilkins⁴, Rupert A.C. Croft³

¹ School of Physics, University of Melbourne, Parkville, VIC 3010, Australia

² ARC Centre of Excellence for All Sky Astrophysics in 3 Dimensions (ASTRO 3D)

³ McWilliams Center for Cosmology, Department of Physics, Carnegie Mellon University, Pittsburgh, PA 15213, USA

⁴ Astronomy Centre, Department of Physics and Astronomy, University of Sussex, Brighton, BN1 9QH, UK

Accepted XXX. Received YYY; in original form ZZZ

ABSTRACT

We examine the properties of the host galaxies of $z = 7$ quasars using the large volume, cosmological hydrodynamical simulation BLUETIDES. We find that the most massive black holes and quasars are hosted by massive galaxies with stellar masses $\log(M_*/M_\odot) = 10.8 \pm 0.2$, and 10.2 ± 0.4 , which have a wide range of star formation rates, of $50_{-35}^{+119} M_\odot/\text{yr}$ and $19_{-12}^{+28} M_\odot/\text{yr}$, respectively. The hosts of the most massive black holes and quasars in BLUETIDES are generally bulge-dominated, with bulge-to-total mass ratio $B/T \simeq 0.85 \pm 0.1$, however their morphologies are not biased relative to the overall $z = 7$ galaxy sample. We find that the hosts of the most massive black holes and quasars are significantly more compact, with half-mass radii $R_{0.5} = 0.29_{-0.10}^{+0.15}$ kpc and $0.28_{-0.06}^{+0.08}$ kpc respectively, relative to galaxies with similar masses, which have $R_{0.5} = 0.5_{-0.2}^{+0.3}$ kpc. We make mock James Webb Space Telescope (JWST) images of these quasars and their host galaxies. We find that distinguishing the host from the quasar emission will be possible but still challenging with JWST, due to the small sizes of quasar hosts. We find that currently observable quasar samples are biased tracers of the intrinsic black hole–stellar mass relations, following a relation that is 0.27 dex higher than that of the full galaxy sample. Finally, we find that black hole hosts are generally quite isolated. However, the most massive black holes are more likely to be found in denser environments than the typical $M_{\text{BH}} > 10^{6.5} M_\odot$ black hole, indicating that minor mergers at least play some role in growing black holes in the early Universe.

Key words: galaxies: quasars: supermassive black holes – galaxies: evolution – galaxies: high-redshift.

1 INTRODUCTION

High-redshift quasars ($z \gtrsim 6$, Fan et al. 2000, 2001, 2003, 2004) are some of the most extreme systems in the Universe, with intense accretion at or even above the Eddington limit (Willott et al. 2010b; Rosa et al. 2011) forming black holes with masses of $10^8 - 10^9 M_\odot$ (Barth et al. 2003; Jiang et al. 2007; Kurk et al. 2007; Rosa et al. 2011) in less than a billion years. These luminous systems are invaluable probes of the early Universe, providing constraints on black hole seed theories (e.g. Mortlock et al. 2011; Volonteri 2012; Bañados et al. 2017), the Epoch of Reionization (e.g. Fan et al. 2006b; Mortlock et al. 2011; Greig & Mesinger 2017; Davies et al. 2018; Greig et al. 2019), and the relation between the growth of black holes and their host galaxies (e.g. Shields et al. 2006; Wang

et al. 2013; Valiante et al. 2014; Schulze & Wisotzki 2014; Willott et al. 2017). The space density of typical Sloan Digital Sky Survey (SDSS) quasars ($M_{\text{UV,AGN}} < -26$) is less than 1 per Gpc³ at $z \gtrsim 6$ (Willott et al. 2010a; Kashikawa et al. 2015; Jiang et al. 2016). Their rarity and extreme properties raise many questions such as ‘Are the biggest black holes found in the rarest, most overdense regions, i.e. the biggest haloes and galaxies (e.g. Springel et al. 2005b; Shen et al. 2007; Fanidakis et al. 2013)?’ and ‘Is this rapid growth driven by galaxy mergers, with hosts that are highly star forming, or are their host galaxies more discy and quiet (e.g. Mor et al. 2012; Netzer et al. 2014; Trakhtenbrot et al. 2018)?’

Understanding the host galaxies of high-redshift quasars is essential for addressing these questions. However, this requires detection and ideally accurate measurements of quasar host galaxies, which is extremely challenging with current telescopes (see e.g. Mechtley et al. 2012). In the rest-frame ultraviolet (UV)/optical, which traces the emission from the accretion disc and the host stel-

★ E-mail: madelinem1@student.unimelb.edu.au (MAM); tiziana@phys.cmu.edu (TDM); swyithe@unimelb.edu.au (JSBW)

lar component, the quasars often outshine their hosts, entirely obscuring the host galaxy emission (Mechtley et al. 2012). The detection of $z \gtrsim 6$ quasar host galaxies has indeed eluded the Hubble Space Telescope. The only current detections of high-redshift quasar hosts are instead in the rest-frame far-infrared, observed in the sub-mm (e.g. Bertoldi et al. 2003; Walter et al. 2003, 2004; Riechers et al. 2007; Wang et al. 2010, 2011; Venemans et al. 2019), which traces cold dust in the host galaxy.

Atacama Large Millimeter Array (ALMA) observations in the sub-mm imply a diverse population of quasar hosts, with inferred dynamical masses of $10^{10} - 10^{11} M_\odot$ (Wang et al. 2013; Venemans et al. 2015; Willott et al. 2017; Trakhtenbrot et al. 2018; Izumi et al. 2018), dust masses of $10^7 - 10^9 M_\odot$ (Venemans et al. 2015; Izumi et al. 2018), sizes of 1-5 kpc (Wang et al. 2013; Venemans et al. 2015; Willott et al. 2017), and a wide range of star-formation rates (SFRs) of $10 - 2700 M_\odot/\text{yr}$ (Venemans et al. 2015; Willott et al. 2017; Trakhtenbrot et al. 2018; Izumi et al. 2018; Shao et al. 2019). The hosts are found in a variety of dynamical states, with some having nearby companions which may suggest a merger system (e.g. Trakhtenbrot et al. 2018), while some show signatures of a rotating disc (e.g. Willott et al. 2017; Trakhtenbrot et al. 2018), or even no ordered motion (Venemans 2017). However, since cold dust may not trace the stellar distribution, there may be significant biases in stellar properties inferred through these observations (e.g. Narayanan et al. 2009; Valiante et al. 2014; Lupi et al. 2019).

Upcoming facilities will provide the next frontier for understanding high-redshift quasars and their host galaxies. Infrared surveys with Euclid (Amiaux et al. 2012) and the Wide Field Infrared Survey Telescope (WFIRST; Spergel et al. 2015) will significantly increase the known sample of $z \gtrsim 6$ quasars. The improved resolution of the James Webb Space Telescope (JWST; Gardner et al. 2006) will allow the first detections of the stellar component of their host galaxies, which will be invaluable for accurately determining the properties of quasar hosts. Making detailed theoretical predictions for the results of these groundbreaking instruments is thus a current priority.

Due to the rarity of high-redshift quasars, comprehensive theoretical predictions require high resolution simulations with large computational volumes. Cosmological hydrodynamical simulations such as Massive Black (Di Matteo et al. 2012), with a volume of (0.76 Gpc)³, and BLUETIDES (Feng et al. 2015), with a volume of (0.57 Gpc)³, have pioneered this area. These simulations have been used to investigate the rapid growth of black holes (Di Matteo et al. 2012; DeGraf et al. 2012b; Feng et al. 2014; Di Matteo et al. 2017) and their relationship to their host galaxies (Khandai et al. 2012; DeGraf et al. 2015; Huang et al. 2018), and make predictions for the highest-redshift quasars that are observed (DeGraf et al. 2012a; Tenneti et al. 2018; Ni et al. 2018).

Previous BLUETIDES analyses were performed with the phase I simulation, which reached a minimum redshift of $z = 8.0$, and BLUETIDES-II, the second phase of the simulation which had been run to $z = 7.5$ when last analysed (Tenneti et al. 2018). In this paper we use the BLUETIDES-II simulation extended further to $z = 7.0$ to make predictions for the properties of quasar host galaxies. At $z = 7.5$, there is one quasar analogue in the BLUETIDES simulation, as studied by Tenneti et al. (2018). Extending the simulation from $z = 7.5$ to 7.0 , a period of only 58 Myr, results in a considerable increase in the number of observable quasar analogues, since this is such an intense growth phase of black holes in the Universe. This statistical sample allows us to make predictions for the broader quasar population, and not just for individual, extreme systems as was possible previously.

The paper is outlined as follows. In Section 2 we describe the simulation and the post-processing used to obtain mock spectra of the quasars and their host galaxies. In Section 3 we consider the intrinsic galaxy properties of the hosts of black holes and quasars. We consider observable properties in Section 4, making spectra and mock JWST images. In Section 5 we examine the black hole–stellar mass relation, showing how observations of these quasars will lead to a biased measurement. We explore the AGN-merger connection in 6, before concluding in Section 7. The cosmological parameters used throughout are from the nine-year Wilkinson Microwave Anisotropy Probe (WMAP; Hinshaw et al. 2013): $\Omega_M = 0.2814$, $\Omega_\Lambda = 0.7186$, $\Omega_b = 0.0464$, $\sigma_8 = 0.820$, $\eta_s = 0.971$ and $h = 0.697$.

2 SIMULATION

2.1 BLUETIDES

The BLUETIDES simulation¹ (Feng et al. 2015) is a cosmological hydrodynamical simulation, which uses the Pressure Entropy Smoothed Particle Hydrodynamics (SPH) code MP-Gadget to model the evolution of 2×7040^3 particles in a cosmological box of volume $(400/h \text{ cMpc})^3$. The mass resolution of the simulation is $1.2 \times 10^7/h M_\odot$ for dark matter particles and $2.4 \times 10^6/h M_\odot$ for gas particles (in the initial condition), with gravitational softening length $\epsilon_{\text{grav}} = 1.5/h \text{ ckpc}$ the effective spatial resolution. From the initial conditions at $z = 99$, BLUETIDES evolved the box to $z = 8$ in phase I (Feng et al. 2015). Phase II of the simulation continued the evolution to $z < 8$, with the first results from this phase given in Tenneti et al. (2018). Here we focus on the lowest redshift currently reached by phase II, $z = 7.0$. From the simulation, we consider the 108000 most massive halos, with masses $M_{\text{vir}} > 10^{10.8} M_\odot$, which contain galaxies with $M_* > 10^{5.9} M_\odot$ and black holes with $M_{\text{BH}} > 10^{5.8} M_\odot$.

BLUETIDES implements a variety of sub-grid physics to model galaxy and black hole formation and their feedback processes. Here we briefly list some of its basic features, and refer the reader to the original paper (Feng et al. 2015) for more detailed descriptions. In the BLUETIDES simulation, gas cooling is performed through both primordial radiative cooling (Katz et al. 1999) and metal line cooling (Vogelsberger et al. 2014). Star formation is based on the multi-phase star formation model originally from Springel & Hernquist (2003) with modifications following Vogelsberger et al. (2013). We also implement the formation of molecular hydrogen and model its effects on star formation using the prescription from Krumholz & Gnedin (2011), where we self-consistently estimate the fraction of molecular hydrogen gas from the baryon column density, which in turn couples the density gradient into the star formation rate. For stellar feedback, we apply a type-II supernova wind feedback model from Okamoto et al. (2010), assuming wind speeds proportional to the local one-dimensional dark matter velocity dispersion. The black hole sub-grid model associated with black hole growth and active galactic nuclei (AGN) feedback are the same as in the MASSIVEBLACK I & II simulations, originally developed in Springel et al. (2005a) and Di Matteo et al. (2005), with modifications consistent with ILLUSTRIS. The large volume of BLUETIDES also allows the inclusion of a model of ‘patchy reionization’ (Battaglia et al. 2013), yielding a mean reionization redshift $z \sim 10$, and incorporating the UV background estimated by Faucher-Giguère et al. (2009).

¹ <http://BlueTides-project.org/>

To extract the properties of galaxies from the simulation, we run a friends-of-friends (FOF) algorithm (Davis et al. 1985). The galaxy properties, such as the star formation density, stellar mass function and UV luminosity function, have been shown to match current observational constraints at $z = 8, 9$ and 10 (Feng et al. 2015; Waters et al. 2016; Wilkins et al. 2017).

To determine the stellar mass of the galaxies from the total stellar mass contained in their host dark matter haloes, we first calculate the galaxy R_{200} , the radius containing 200 times the critical stellar mass density (the critical density of the Universe multiplied by the baryon fraction and star formation efficiency of the simulation). This restricts the calculation to the local density peak around the galaxy, ensuring that the mass from neighbouring galaxies is excluded. We then calculate the half-mass radius inside this R_{200} , $R_{0.5}$. We define the stellar mass of a galaxy as the mass contained within $3R_{0.5}$ (as in, e.g. Tacchella et al. 2019).

We determine the morphology of the galaxy by its bulge-to-total ratio, calculated using the bulge-to-disc decomposition method of Scannapieco et al. (2009). We first construct a circularity parameter $\epsilon = j_z/j_{\text{circ}}(r)$ for each star particle in the galaxy, where j_z is the projection of the specific angular momentum of the star particle in the direction of the total angular momentum of the galaxy, and $j_{\text{circ}}(r)$ is the angular momentum expected for a circular orbit at the radius r : $j_{\text{circ}} = rv_{\text{circ}}(r) = \sqrt{GM(<r)r}$. We identify star particles with $\epsilon > 0.7$ as disc stars, and define the bulge-to-total ratio as $B/T = 1 - f_{\epsilon > 0.7}$ where $f_{\epsilon > 0.7}$ is the fraction of disc stars in the galaxy.

2.2 Mock spectra

2.2.1 Galaxy SEDs

To determine the spectral energy distribution (SED) of a galaxy, we assign a SED from a simple stellar population (SSP) to each star particle based on its mass, age and metallicity. We do this using the Binary Population and Spectral Population Synthesis model (BPASS, version 2.2; Stanway & Eldridge 2018), assuming a modified Salpeter initial mass function with a high-mass cut-off of $300M_{\odot}$. The SED of the galaxy is taken as the sum of the SEDs of each of its star particles. To determine the relative contribution of the stellar and nebular emission, we assume an escape fraction of 0.9.

2.2.2 Quasar spectra

To assign spectra to each of our quasars, we use the CLOUDY spectral synthesis code (Ferland et al. 2017), as in Tenneti et al. (2018).

The continuum is given by

$$f_{\nu} = \nu^{\alpha_{\text{UV}}} \exp\left(\frac{-h\nu}{kT_{\text{BB}}}\right) \exp\left(\frac{-kT_{\text{IR}}}{h\nu}\right) + a\nu^{\alpha_{\text{X}}} \quad (1)$$

where $\alpha_{\text{UV}} = -0.5$, $\alpha_{\text{X}} = -1$, $kT_{\text{IR}} = 0.01\text{Ryd}$, and T_{BB} is the temperature of the accretion disc, which is determined by the black hole mass and its accretion rate

$$T_{\text{BB}} = \left(\frac{3c^6}{8\pi^6 \sigma_{\text{SB}} G^2} \frac{M_{\text{BH}}}{M_{\text{BH}}^2} \right)^4 = 2.24 \times 10^9 \left(\frac{M_{\text{BH}}}{M_{\odot}/\text{yr}} \right)^4 \left(\frac{M_{\text{BH}}}{M_{\odot}} \right)^{-8} \text{K.} \quad (2)$$

The normalisation of the continuum is set by the bolometric luminosity of the quasar, $L_{\text{AGN}} = \eta M_{\text{BH}} c^2$, where we assume an efficiency $\eta = 0.1$.

The emission lines are calculated with CLOUDY assuming a hydrogen density of 10^{10}cm^{-3} at the face of the cloud, which has inner radius 10^{18}cm , and a total hydrogen column density of 10^{10}cm^{-2} .

We also implement Lyman-forest extinction on the redshifted spectra (Madau 1995; STScI Development Team 2018) for both the quasars and the host galaxies.

2.2.3 Dust attenuation and extinction

As in Wilkins et al. (2017), we model the dust attenuation of galaxies by relating the density of metals along a line of sight to the UV-band dust optical depth τ_{UV} . For each star particle in the galaxy, we calculate $\tau_{\text{UV},*}$ as

$$\tau_{\text{UV},*} = -\kappa \Sigma(x, y, z) \left(\frac{\lambda}{5500\text{\AA}} \right)^{\gamma}, \quad (3)$$

where $\Sigma(x, y, z) = \int_{z'=0}^z \rho_{\text{metal}}(x, y, z') dz'$ is the metal surface density at the position of the star particle, along the z -direction line of sight, and κ and γ are free parameters. Here we use $\kappa = 10^{4.6}$ and $\gamma = -1.0$, which are calibrated against the observed galaxy UV luminosity function at redshift $z = 7$. The total dust-attenuated galaxy luminosity is the sum of the extincted luminosities of each individual star particle.

We apply the same technique to determine the dust attenuation of the AGN, with the dust optical depth calculated using the metal column density integrated along a line of sight to the quasar:

$$\tau_{\text{UV,AGN}} = \kappa \int_{\text{ray}} \rho_{\text{metal}}(l) dl \left(\frac{\lambda}{5500\text{\AA}} \right)^{\gamma}, \quad (4)$$

with the same value of κ and γ (see also Ni, Matteo, Gilli, Croft, Feng & Norman Ni et al.). Dust attenuation of the AGN mainly traces the regions of high gas density near the centre of the galaxy, with the gas metallicity Z only modulating the dust extinction at a sub-dominant level (see Figure 14 in Ni, Matteo, Gilli, Croft, Feng & Norman Ni et al., for illustration.). Because of the angular variation in the density field surrounding the central black hole, the dust extinction for AGN is sensitive to the choice of line of sight, unlike for galaxies, whose dust attenuation is accumulated over the extended source. For each quasar we therefore calculate $\tau_{\text{UV,AGN}}$ along approximately 1000 lines of sight. See Ni, Matteo, Gilli, Croft, Feng & Norman (Ni et al.) for full details.

3 PROPERTIES OF BLACK HOLE HOST GALAXIES

3.1 Sample selection

The black hole population in BLUETIDES at $z = 7.0$ is presented in Figure 1, which shows the distributions of their masses and luminosities, as well as the quasar UV luminosity function. By considering the UV-band dust extinction as described in Section 2.2.3 and Ni, Matteo, Gilli, Croft, Feng & Norman (Ni et al.), BLUETIDES produces a luminosity function that is marginally consistent with the high-redshift observations—BLUETIDES predicts the expected number density of observed high- z quasars. The most massive black holes in BLUETIDES at $z = 7$ have masses of $M_{\text{BH}} \simeq 10^{8.5}M_{\odot}$, and the most luminous black holes have intrinsic bolometric luminosities $L_{\text{bol}} \simeq 10^{47}\text{erg s}^{-1} \simeq 10^{13}L_{\odot}$, equivalent to those of the faintest observed high- z quasars.

From this black hole population we select three samples; the most massive black holes, ‘quasars’, and ‘hidden quasars’.

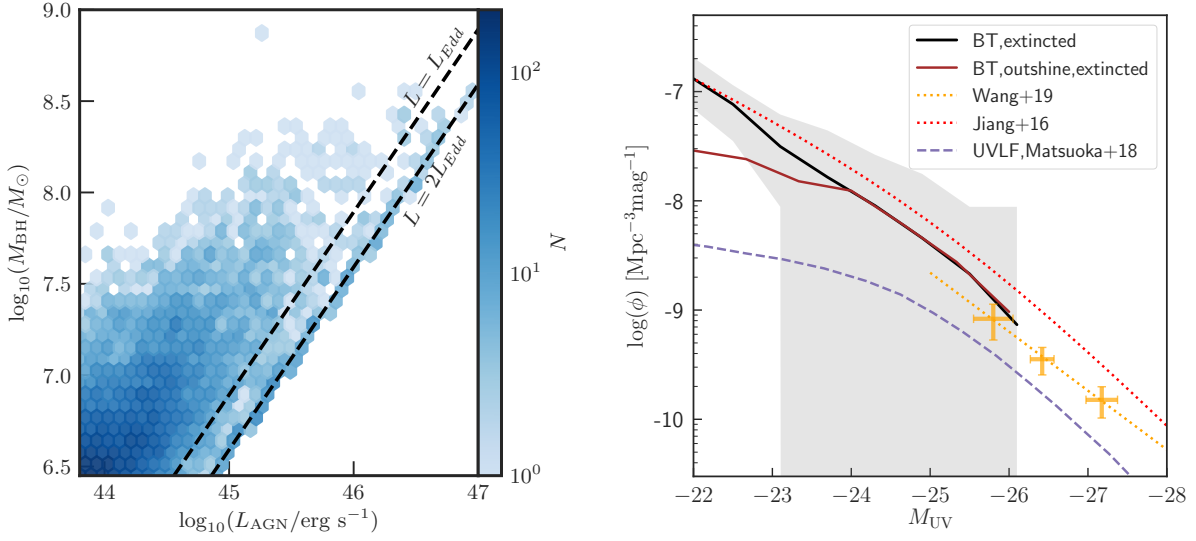


Figure 1. *Left:* The distribution of black hole masses and AGN bolometric luminosities for BLUETIDES galaxies at $z = 7$ (blue density plot). The Eddington limit is shown for reference (dashed black line), as well as twice the Eddington limit, which is the upper limit of the black hole accretion rate set in the simulation. *Right:* The UV-band luminosity function of AGN at $z = 7$. The black solid line is the dust-extincted quasar luminosity function from BLUETIDES. The brown solid line is the luminosity function including only the AGN that can outshine their host galaxies. The grey shaded area gives the error estimate by considering the dust extinction through all lines of sight of the AGN population. The orange solid symbols with error bars show the measured binned quasar luminosity function from Wang et al. (2018) at $z \sim 6.7$. The red dotted line is the $z \sim 6$ fitted quasar luminosity function measured by Jiang et al. (2016). The purple dashed line gives the luminosity function from Matsuoka et al. (2018b), based on the population of $5.7 < z < 6.5$ quasars and extrapolated to $z = 7$.

Massive black hole sample: We consider the ten most massive black holes at $z = 7$, which have masses $M_{\text{BH}} = 10^{8.44} - 10^{8.89} M_{\odot}$, to be our ‘massive black hole’ sample.

Quasar sample: To select ‘quasars’ from the simulation, we consider the galaxy and AGN UV-band absolute magnitudes, as shown in Figure 2. We make the simple assumption that every black hole with $M_{\text{UV,AGN}} < M_{\text{UV,Host}}$ would be classified as a quasar, since the AGN outshines the host galaxy. This results in a sample of 191 BLUETIDES quasars, which is only 2 per cent of the black holes with $M_{\text{BH}} > 10^{6.5} M_{\odot}$ (see Figure 2). We note that the assumption that $M_{\text{UV,AGN}} < M_{\text{UV,Host}}$ for a galaxy to be classified as a quasar is not an accurate representation of the true observational quasar selection techniques, and may underestimate the number of galaxies in our sample that would be observed as quasars.

Hidden quasar sample: Within our simulation, 67.5 per cent of black holes brighter than the WFIRST detection limit of $m_{\text{UV}} < 26.9$ ($L_{\text{AGN}} > 10^{45.2} \text{ erg s}^{-1}$ at $z = 7$) have host luminosities that outshine the AGN. These black holes are experiencing significant black hole growth, with high AGN luminosities, but are simply ‘hidden’ by their luminous host galaxies. We consider all black holes with intrinsic luminosities $L_{\text{AGN}} > 10^{45.2} \text{ erg s}^{-1}$ and with $M_{\text{UV,AGN}} > M_{\text{UV,Host}}$ as ‘hidden’ quasars, i.e. those outshined by their host galaxy.

3.2 Galaxy properties

We now investigate the properties of the hosts of the most massive black holes and quasars in BLUETIDES at $z = 7$.

In Figure 3 we show the relation between AGN luminosity and both stellar mass and star formation rate at $z = 7$. The most massive black holes are in massive galaxies with stellar masses

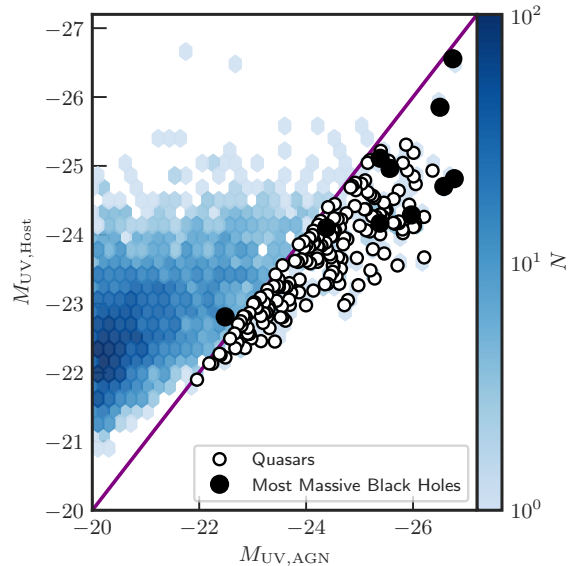


Figure 2. The distribution of host and AGN absolute intrinsic UV magnitudes for BLUETIDES galaxies at $z = 7$ (blue density plot). We classify quasars (white circles) as those with $M_{\text{UV,AGN}} < M_{\text{UV,Host}}$, since the AGN outshines the host galaxy. The 10 most massive black holes (black circles) are also shown.

$\log(M_{*}/M_{\odot}) = 10.76^{+0.18}_{-0.16}$, which have a wide range of star forma-

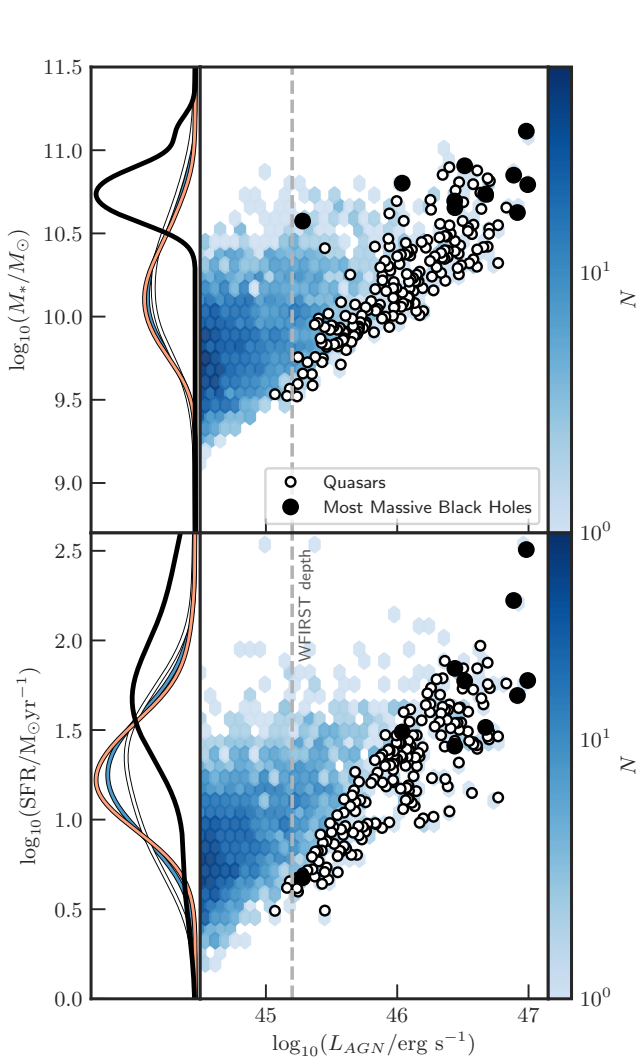


Figure 3. The relations between AGN luminosity and stellar mass (upper right panel) and star formation rate (lower right panel). The blue density plot shows the distribution for all BLUETIDES galaxies, with the most massive black holes and quasars also plotted (see legend). The left panels show the distributions of the host properties for the most massive black holes (black line), quasars (white line), hidden quasars (salmon line), and for all black holes with $L_{\text{AGN}} > 10^{45.2} \text{ erg s}^{-1}$ (the WFIRST detection limit; blue line). The WFIRST detection limit is shown in the right panels for reference (grey dashed line).

tion rates, $50^{+119}_{-35} M_{\odot}/\text{yr}^2$.² We find that the quasar hosts also have large but lower stellar masses of $\log(M_{*}/M_{\odot}) = 10.21^{+0.40}_{-0.37}$, and lower star formation rates of $19^{+28}_{-12} M_{\odot}/\text{yr}$. From Figure 3 we see that, on average, lower luminosity quasars have less extreme host galaxies, with lower masses and star formation rates.

² Errors presented in this manner correspond to the 16th and 84th percentiles of the distributions, relative to the median value

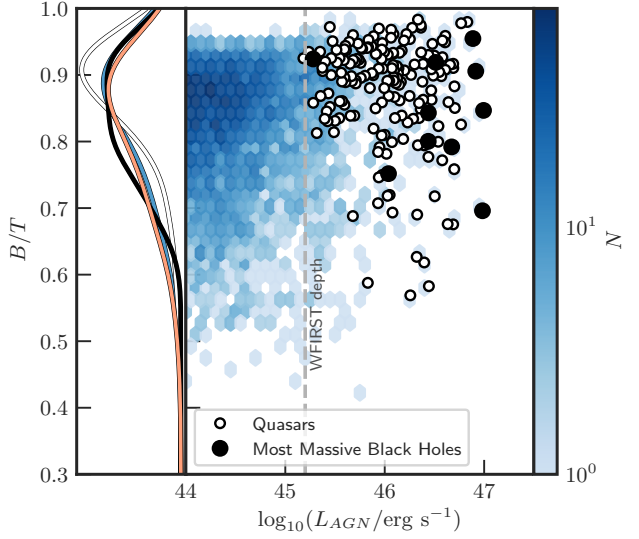


Figure 4. The relation between the ratio of stellar mass contained in a galaxy's bulge to its total stellar mass (B/T) and AGN luminosity. The blue density plot shows the distribution for all BLUETIDES galaxies, with the most massive black holes and quasars also plotted (see legend). The left panel shows the distribution of B/T for the most massive black holes (black line), quasars (white line), hidden quasars (salmon line), and all black holes brighter than $L_{\text{AGN}} > 10^{45.2} \text{ erg s}^{-1}$ (blue line). $L_{\text{AGN}} = 10^{45.2} \text{ erg s}^{-1}$ (the WFIRST detection limit) is shown in the right panel for reference (grey dashed line).

Figure 3 also shows the one-dimensional distributions of stellar mass and star formation rate for these samples, alongside all black holes brighter than $L_{\text{AGN}} > 10^{45.2} \text{ erg s}^{-1}$, and ‘hidden’ quasars. This shows that the most massive black holes live in more massive galaxies, with higher star formation rates, than the total sample of bright black holes ($L_{\text{AGN}} > 10^{45.2} \text{ erg s}^{-1}$), which have $\log(M_{*}/M_{\odot}) = 10.16^{+0.36}_{-0.32}$ and star formation rates of $18^{+22}_{-10} M_{\odot}/\text{yr}$. The hidden quasars are hosted by galaxies with $\log(M_{*}/M_{\odot}) = 10.14^{+0.34}_{-0.31}$ and star formation rates of $18^{+19}_{-9} M_{\odot}/\text{yr}$.

At a fixed quasar luminosity, the quasars are hosted by less massive galaxies with lower star formation rates than the hidden quasars. This is expected due to the $M_{\text{UV,AGN}} < M_{\text{UV,Host}}$ selection: the quasar sample contains galaxies with lower $M_{\text{UV,Host}}$ for fixed $M_{\text{UV,AGN}}$, which is produced by having a lower star formation rate. Galaxies with higher star formation rates have higher luminosities which outshine their quasar, resulting in ‘hidden’ quasars of the same quasar luminosity. As stellar mass is an integrated quantity, the selection effect is weakened slightly.

In Figure 4 we show the relation between AGN luminosity and the ratio of stellar mass contained in a galaxy's bulge to its total stellar mass (B/T). The hosts of the most massive black holes and quasars all show bulge-dominated morphologies, although there is a large tail to lower B/T , with $B/T = 0.85^{+0.09}_{-0.10}$, and $0.89^{+0.07}_{-0.10}$ for the two samples respectively. Their morphologies have a similar distribution to that of the total sample of bright black holes ($L_{\text{AGN}} > 10^{45.2} \text{ erg s}^{-1}$), with $B/T = 0.86^{+0.09}_{-0.13}$, and hidden quasars, with $B/T = 0.84^{+0.10}_{-0.14}$. The hosts of the most massive black holes and quasars in BLUETIDES are generally bulge-dominated, but

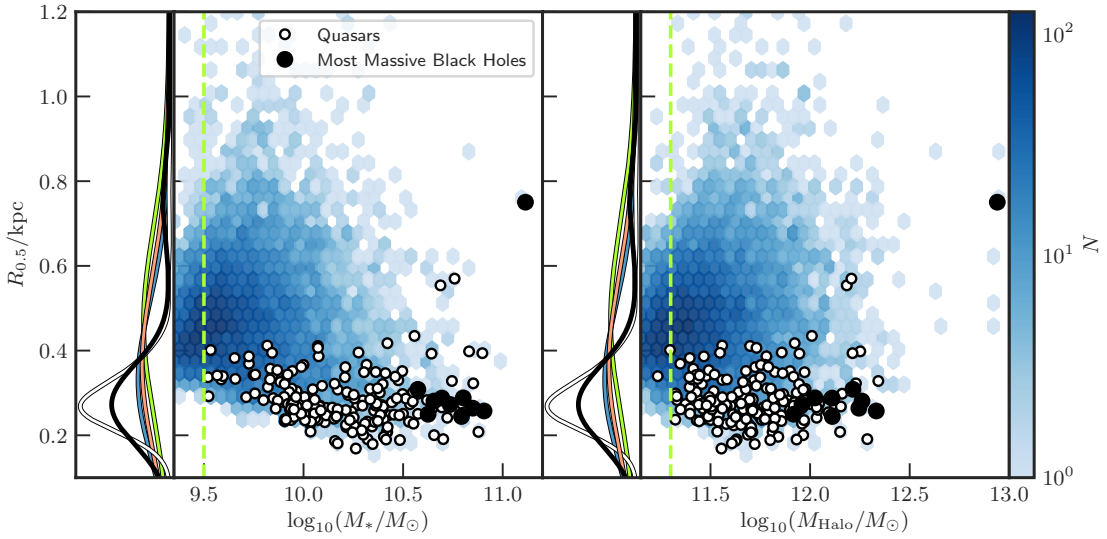


Figure 5. The relation between half-mass radius and stellar and halo mass. The blue density plot shows the distribution for all BLUETIDES galaxies, with the most massive black holes and quasars also plotted (see legend). The thin panels show the distributions of half-mass radius for the most massive black holes (black line), quasars (white line), hidden quasars (salmon line), all black holes brighter than $L_{\text{AGN}} > 10^{45.2} \text{ erg s}^{-1}$ (blue line) and the total sample of galaxies with $M_* > 10^{9.5} M_\odot$, and $M_{\text{Halo}} > 10^{11.3} M_\odot$ (green line). $M_* = 10^{9.5} M_\odot$ and $M_{\text{Halo}} = 10^{11.3} M_\odot$ are shown for reference (green dashed line).

are not biased in morphology relative to the overall galaxy sample at $z = 7$.

Lupi et al. (2019) performed a high-resolution cosmological zoom-in simulation of a halo containing a black hole with mass $M_{\text{BH}} = 10^{8.9} M_\odot$ at $z = 7$, similar to that of the most massive black hole in BLUETIDES. They found its host galaxy to have a mass of $M_* \simeq 10^{11} M_\odot$ and a large star formation rate of $\sim 10^{2.5} M_\odot/\text{yr}$ at $z = 7$, equivalent to the most massive and star forming galaxies in BLUETIDES. Their quasar host is less bulge-dominated than those in our quasar sample, with a bulge-to-total mass ratio of $B/T \sim 0.45$. This is potentially due to the increased resolution of their simulation, which has the ability to better resolve the disc structure. The results of Lupi et al. (2019) are therefore reasonably consistent with the BLUETIDES simulation, given their sample of only one quasar host.

Figure 5 shows the relation between half-mass radius $R_{0.5}$ and both stellar and halo mass. The most massive black hole hosts have small radii of $R_{0.5} = 0.29^{+0.15}_{-0.10}$ kpc, and the quasar hosts $R_{0.5} = 0.28^{+0.08}_{-0.06}$ kpc. The total sample of bright black holes ($L_{\text{AGN}} > 10^{45.2} \text{ erg s}^{-1}$) have much larger sizes of $R_{0.5} = 0.39^{+0.28}_{-0.17}$ kpc, as do hidden quasars, which have $R_{0.5} = 0.43^{+0.32}_{-0.19}$ kpc, and galaxies with similar masses ($M_{\text{Halo}} > 10^{11.3} M_\odot$ and $M_* > 10^{9.5} M_\odot$), which have $R_{0.5} = 0.5^{+0.3}_{-0.2}$ kpc. A distinguishing feature of massive black hole and quasar hosts is therefore that they are very compact.

4 QUASAR OBSERVATIONS

In Section 3, we considered the properties of the host galaxies of the most massive black holes and intrinsically bright quasars in the BLUETIDES simulation. We now consider the effects of dust-attenuation and survey magnitude limits to mimic true quasar observations, to make predictions for upcoming observations with JWST.

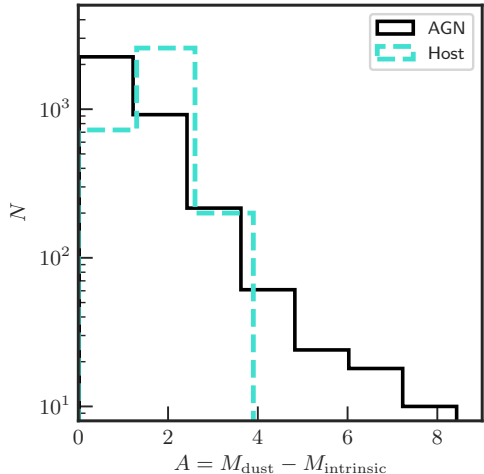


Figure 6. The distributions of dust extinction $A = M_{\text{dust}} - M_{\text{intrinsic}}$ applied to galaxies and AGN. We take the dust extinction for the AGN as that along the line of sight with the least dust-extinction, which is typically the face-on direction, as an optimistic assumption.

4.1 Observable quasar sample selection

4.1.1 Magnitude limits of quasar observations

To select our observable quasar samples, we first consider the magnitude limits of various observational surveys.

The most well-known sample of high- z quasars is that of the Sloan Digital Sky Survey (SDSS; e.g. Fan et al. 2003, 2006a; Jiang et al. 2016). The faintest quasar in this sample is SDSS J0129-0035, with $m_{1450} = 22.8$, or $M_{1450} = -23.89$ at $z = 5.78$ (Wang

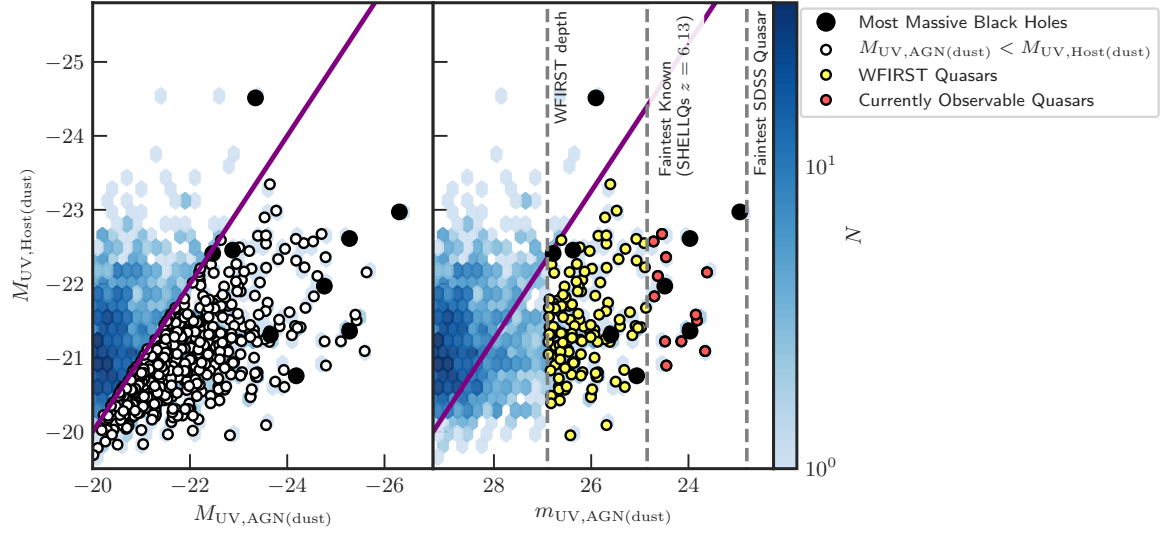


Figure 7. The distribution of galaxy and AGN dust-attenuated UV magnitudes for BLUETIDES galaxies at $z = 7$ (blue density plot). The left panel shows the absolute host and AGN magnitudes, and the right shows the apparent AGN magnitude for comparison with observational detection limits. Using the left panel we classify quasars as those with $M_{\text{UV,AGN(dust)}} < M_{\text{UV,Host(dust)}}$, since the AGN outshines the host galaxy. Using the observational detection limits shown in the right panel, we further split the quasars into the currently observable quasar and WFIRST quasar samples. The most massive black holes are also shown.

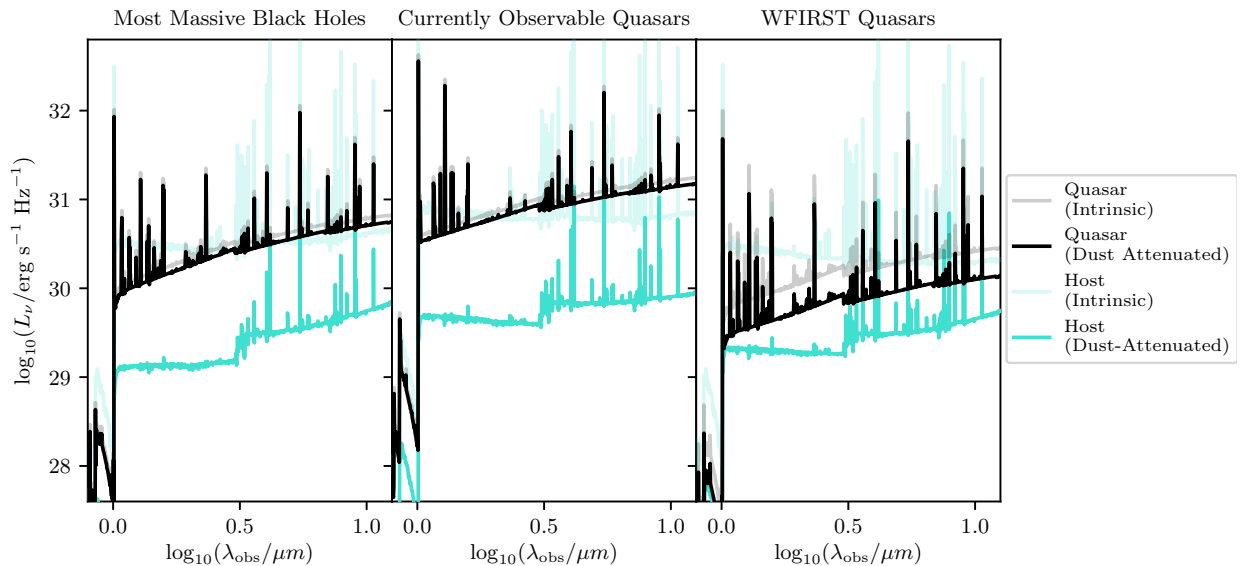


Figure 8. The spectra of a quasar and its host galaxy, for the median mass black hole in the most massive black hole sample (left), and the median luminosity black hole in the currently observable (middle) and WFIRST (right) quasar samples. The upper grey curves show the intrinsic quasar spectra, whilst the lower black curves shows the quasar spectra with our dust extinction law applied. The upper turquoise curves show the intrinsic host galaxy spectra, whilst the lower turquoise curves show the host galaxy spectra with our dust extinction law applied.

et al. 2013; Bañados et al. 2016). This is of similar luminosity to the brightest quasars in the BLUETIDES simulation at $z = 7$.

The faintest high- z quasars observed to date are those discovered in the Subaru High- z Exploration of Low-Luminosity Quasars (SHELLQs) project (Matsuoka et al. 2018a), which uses imaging from the Subaru Hyper Suprime-Cam and follow-up spectroscopy using the Gran Telescopio Canarias and the Subaru Telescope. This

sample includes $5.7 < z < 6.8$ quasars down to magnitudes of $m_{1450} = 24.85$, or $M_{1450} = -21.93$ (HSC J1423–0018 at $z = 6.13$).

At the forefront of upcoming high-redshift quasar discovery surveys is the WFIRST High Latitude Survey, which will cover 2,000 square degrees to a magnitude of 26.9 in the Y , J and H bands (Spergel et al. 2015). We assume that there will be some bluer comparison data of significant depth which can be used to se-

lect dropouts, so take $m_{1450} = 26.9$ as the faintest AGN luminosity that could be detected by WFIRST.

4.1.2 Observable Quasars

In Section 3 we selected our quasar sample based on the intrinsic UV-band magnitudes of the black holes and host galaxies (Figure 2), with ‘quasars’ defined as black holes which had intrinsic magnitudes brighter than their hosts. In Figure 6 we show the difference between dust-attenuated and intrinsic magnitudes for both AGN and host galaxies, $A = M_{\text{dust}} - M_{\text{intrinsic}}$, as calculated following the procedures outlined in Section 2.2.3. Here, and throughout the remainder of this paper, we take the dust extinction for the AGN as that along the line-of-sight with the minimum $\tau_{\text{UV,AGN}}$, as an optimistic estimate of the AGN dust extinction. This generally corresponds to the face-on direction (see Ni, Matteo, Gilli, Croft, Feng & Norman Ni et al.).

Figure 6 shows that AGN and host galaxies experience a similar level of dust attenuation in the majority of cases. The AGN population, however, exhibits a small tail in the distribution extending to large A . These AGN with extreme dust attenuation are a mixed population of black holes, with a variety of masses and accretion rates. This extinction results in some of the ‘intrinsic quasars’ having dust-attenuated AGN magnitudes that no longer outshine their host galaxy. It is therefore important when making mock observational samples to select them based on their dust-attenuated magnitudes.

In Figure 7 we show the relation between galaxy and AGN UV dust-attenuated magnitudes for the BLUETIDES galaxies. Since surveys are limited by apparent and not absolute magnitude, we convert our AGN magnitudes to $m_{\text{UV,AGN}}$ using $m - M = 49.25$, and overplot the observational selection limits described in 4.1.1.

As in Section 3, we make the simple assumption that AGN which outshine their host galaxy in the UV-band are classified as ‘quasars’. In contrast to Section 3, however, we perform this classification using dust-attenuated magnitudes: ‘quasars’ are black hole with $M_{\text{UV,AGN(dust)}} < M_{\text{UV,Host(dust)}}$. Using the limiting magnitudes from SHELLQs and WFIRST, we define our two observable quasar samples as:

- Currently observable quasars: $M_{\text{UV,AGN(dust)}} < M_{\text{UV,Host(dust)}}$ and $m_{\text{UV,AGN(dust)}} < 24.85$
- WFIRST quasars: $M_{\text{UV,AGN(dust)}} < M_{\text{UV,Host(dust)}}$ and $24.85 < m_{\text{UV,AGN(dust)}} < 26.9$

The ‘currently observable’ and ‘WFIRST’ quasar samples contain 17 and 137 quasars respectively, which is all black holes in the simulation with $m_{\text{UV,AGN(dust)}} < 24.85$, and 93 per cent of black holes with $24.85 < m_{\text{UV,AGN(dust)}} < 26.9$ (see Figure 2). Defining the observable quasar samples using the dust attenuated magnitudes therefore selects a different, but similarly-sized sample of black holes. The spectra of the black holes with the median AGN luminosity from these two quasar samples are shown in Figure 8 as examples, alongside that of the median mass black hole from the most massive black hole sample.

4.2 Images of quasar hosts

To visualize the host galaxies of the most massive black holes and ‘currently observable’ and ‘WFIRST’ quasars, we first make im-

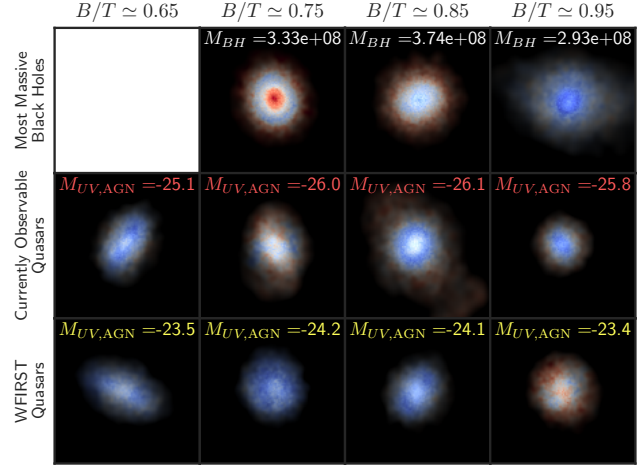


Figure 9. The stellar mass distribution of four BLUETIDES galaxies from each of the most massive black hole, currently observable quasar, and WFIRST quasar samples, selected to show a range of morphologies ($B/T \simeq 0.65, 0.75, 0.85$ and 0.95 ; left to right shows more disc-like to more bulge-dominated galaxies). The minimum B/T for the most massive black hole sample is ~ 0.70 and so only three galaxies from that sample are shown. Each galaxy is viewed face-on, with a field-of-view of 3 kpc. The colour depicts the age of the stellar population, from bluest (≤ 20 Myr) to reddest (≥ 220 Myr), with a linear scale.

ages of their mass distributions using GAEPSI2,³ a suite of routines for visualizing SPH simulations. We select four galaxies from each sample with a representative range of morphologies ($B/T \simeq 0.65, 0.75, 0.85$ and 0.95) to image. We note that the minimum B/T for the most massive black hole sample is $\simeq 0.70$ and so we only select three galaxies from that sample. The mass distributions of these sample galaxies from a face-on and edge-on perspective are shown in Figures 9 and 10 respectively, with colours depicting stellar age. These images show a variety of sizes, shapes and ages of the black hole and quasar host galaxies.

We also construct a matched sample for comparison with the three representative most massive black hole hosts. These matched galaxies are chosen to have small black holes, $10^{6.5} < M_{\text{BH}}/M_{\odot} < 10^7$, but the most similar stellar mass and B/T to that of the three most massive black hole hosts. Images of these representative most massive black holes and the matched galaxy sample can be seen in Figure 11. The galaxies in the matched sample are more diffuse and slightly more extended than the hosts of the most massive black holes. This is consistent with our findings from Figure 5, which shows that the hosts of massive black holes are more compact than other galaxies of equivalent stellar mass.

We produce mock JWST images using SYNTHOBS,⁴ a package for producing synthetic observations from SPH simulations. SYNTHOBS takes the flux of each stellar particle, applies the specified photometric filter, and convolves this emission with the corresponding JWST point-spread function (PSF). We assume that the quasar emission comes from a single point, with the quasar thus appearing as a point source convolved with the PSF in the images. By applying the appropriate smoothing, SYNTHOBS produces a mock image with the pixel scale of the instrument. Dust-attenuation is applied

³ <https://github.com/rainwoodman/gaepsi2>

⁴ <https://github.com/stephenmwilkins/SynthObs>

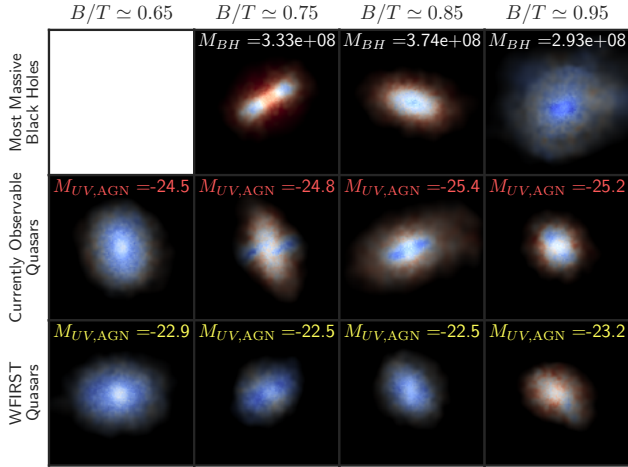


Figure 10. The stellar mass distribution of four BLUETIDES galaxies from each of the most massive black hole, currently observable quasar, and WFIRST quasar samples, selected to show a range of morphologies ($B/T \simeq 0.65, 0.75, 0.85$ and 0.95 ; left to right shows more disc-like to more bulge-dominated galaxies). The minimum B/T for the most massive black hole sample is ~ 0.70 and so only three galaxies from that sample are shown. Each galaxy is viewed edge-on, with a field-of-view of 3 kpc. The colour depicts the age of the stellar population, from bluest (≤ 20 Myr) to reddest (≥ 220 Myr), with a linear scale.

following the methodology described in Section 2.2.3, and we use the minimum AGN dust attenuation of the various sight-lines. We do not include the effect of noise.

In Figure 12 we show mock JWST imaging in the NIRCam F115W filter of the galaxies hosting the median mass black hole in the most massive black hole sample, and the median luminosity black holes in the currently observable and WFIRST quasar samples (i.e. those whose spectra are shown in Figure 8). We show images with and without dust attenuation, and with and without the quasar emission. With a resolution of 0.031 arcseconds, JWST only partially resolves the host galaxies, with diameters of ~ 0.6 kpc or ~ 0.1 arcseconds at $z = 7$. Their emission is centrally concentrated, and so the hosts appear as a smeared PSF at this resolution. However, as the density of dust is highest in the central regions, the dust attenuated images show more interesting, asymmetrical features. These images clearly show that the host galaxy of the sample currently observable quasar has an extended feature, suggesting a potential recent or ongoing merger.

The limited resolution of these small galaxies makes it difficult to distinguish the host galaxy once the point-source quasar emission is included in the images. For the intrinsic images, the image is broader than the quasar image (i.e. the PSF of the telescope), suggesting that an accurate modelling technique should be able to detect the host emission despite the presence of the quasar. However, including the effect of dust-attenuation makes the host more difficult to distinguish from the quasar, as its emission becomes fainter and less extended. The brightness contrast between the host and quasar is ~ 1.5 orders of magnitude at the centre, decreasing with distance from the quasar, with the two having similar brightnesses towards the edge of the host galaxy at $\sim 0.5''$. Distinguishing the host galaxy from the quasar emission will therefore still be challenging with JWST, even with its improved resolution over the Hubble Space Telescope. However, extended structures,

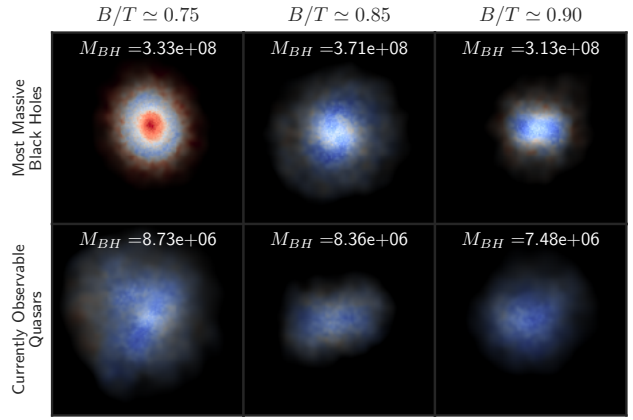


Figure 11. The stellar mass distribution of three BLUETIDES galaxies from the most massive black hole sample, alongside a matched sample of galaxies with a similar stellar mass and bulge-to-total ratio, but low black hole masses. Each galaxy is viewed face-on, with a field-of-view of 3 kpc. The colour depicts the age of the stellar population, from bluest (≤ 20 Myr) to reddest (≥ 220 Myr), with a linear scale.

like that seen in the host of the sample currently observable quasar, could more easily be detected.

We show mock JWST images of the sample most massive black hole in all of the NIRCam wide-band filters red-ward of the Lyman-break in Figure 13. As the wavelength increases, the resolution of the telescope decreases. Thus, whilst the contrast ratio of the quasar and its host should be lower at larger wavelengths due to the spectral shapes of quasars and host galaxies (see Figure 8), redder NIRCam filters do not make the host more easily distinguishable.

In addition to producing images of the median mass and luminosity black holes in the most massive black hole and quasar samples (Figure 12), we also consider the black hole in each sample which has the lowest contrast ratio between the AGN and host luminosity, $M_{\text{UV,Host(dust)}} - M_{\text{UV,AGN(dust)}}$ (with $M_{\text{UV,AGN(dust)}} < M_{\text{UV,Host(dust)}}$). Mock JWST images of these black holes are shown in Figure 14. The host galaxies of these black holes are much easier to distinguish from the quasar point source emission, particularly for the sample most massive black hole and WFIRST quasar, which have the lowest contrast ratios of $\simeq 0.05$. Thus, while the host galaxies of quasars will still be difficult to detect with JWST in general, it should be possible to detect the hosts of quasars with low contrast ratios.

5 BIASES IN THE OBSERVED SCALING RELATIONS

In Figure 15, we show the $z = 7$ black hole–stellar mass and black hole–bulge mass relations as predicted by BLUETIDES. The best-fitting relations for black holes with $M_{\text{BH}} > 10^{6.5} M_{\odot}$ are

$$\log(M_{\text{BH}}/M_{\odot}) = (1.32 \pm 0.02) \log(M_{*}/M_{\odot}) - (6.0 \pm 0.2), \quad (5)$$

and

$$\log(M_{\text{BH}}/M_{\odot}) = (1.50 \pm 0.03) \log(M_{\text{Bulge}}/M_{\odot}) - (7.7 \pm 0.3). \quad (6)$$

There is a scatter of 0.2 dex in both relations, so the simulation shows no preference for a tighter correlation of black hole mass with either total or bulge stellar mass. We note that the black hole–bulge relation is steeper than the local relation (Kormendy & Ho

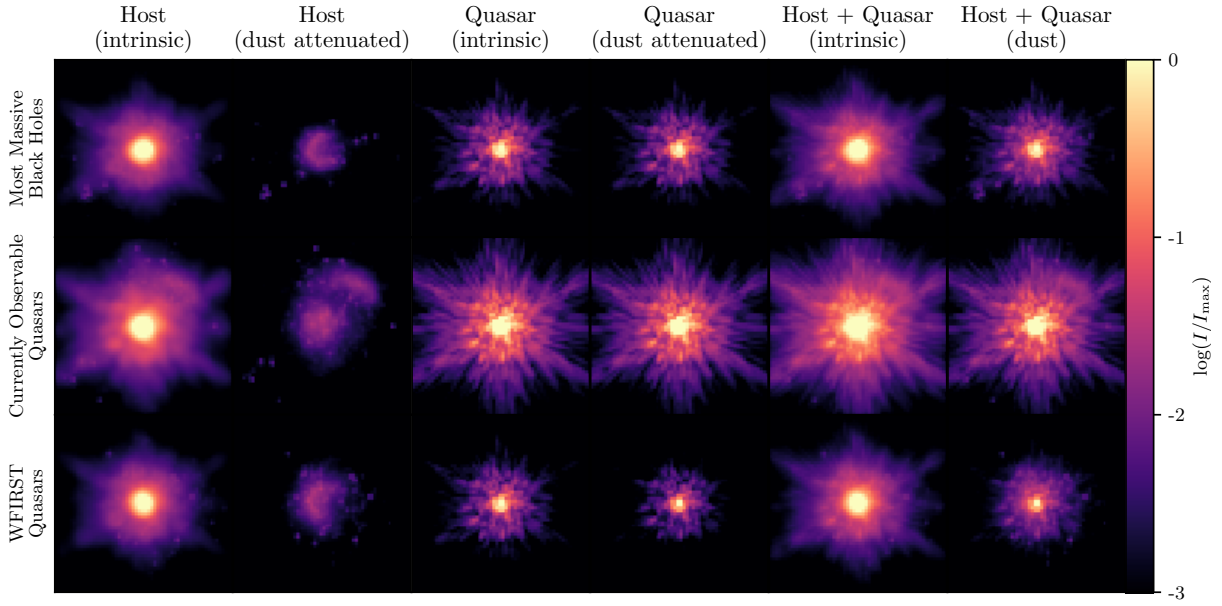


Figure 12. Simulated face-on images of BLUETIDES galaxies in the JWST NIRCam F115W filter, showing one galaxy from each black hole sample. The galaxy displayed from the most massive black hole sample has the black hole with the median black hole mass, while the galaxies displayed from the two quasar samples are those with the median AGN luminosity (i.e. the galaxies whose spectra is shown in Figure 8). The host galaxy emission is shown with and without dust-attenuation in the two left-most columns. The emission from the quasar is shown with and without dust-attenuation in the middle columns, with the combined quasar and host galaxy image shown with and without dust attenuation (applied to both the host and quasar) in the right-most panels. The field-of-view is 10kpc, or 1.86''. Note that all panels are shown with the same intensity scale.

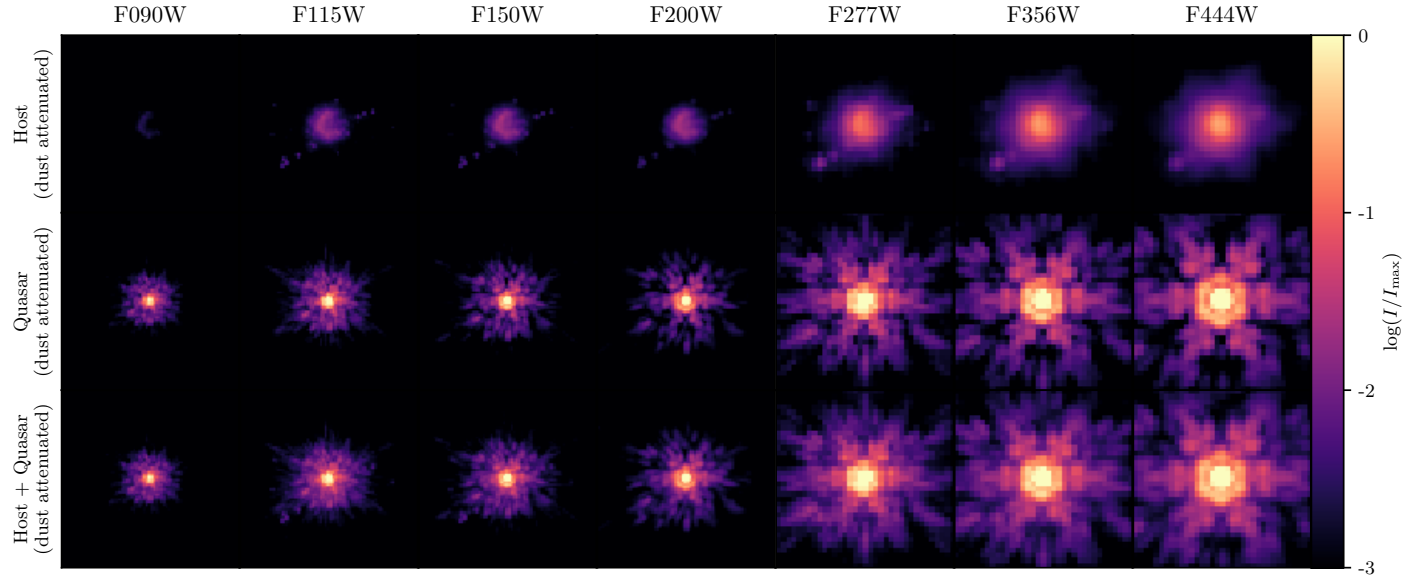


Figure 13. Simulated face-on images of the sample galaxy from the most massive black hole sample in the JWST NIRCam wide-band filters. The host galaxy emission is shown in the top panels, the emission from the quasar in the middle panels, with the combined quasar and host galaxy image shown in the bottom panels. All images include dust extinction of both the quasar and the host galaxy. The field-of-view is 12kpc, or 2.23''. Note that all panels are shown with the same intensity scale.

2013), which is also shown in Figure 15. However, the simulations and local observations are reasonably consistent, particularly at the highest masses where the observed relation is best measured.

In Figure 16 we plot the black hole–stellar mass relation for the most massive black holes, currently observable quasars, and

WFIRST quasars. These all show black hole mass distributions that are skewed to higher masses than the total sample of galaxies with $M_* > 10^{10} M_\odot$, as seen in the left panel of Figure 16; the hosts of the most massive black holes and quasars have large black hole masses for their stellar mass. To investigate the effect of this bias

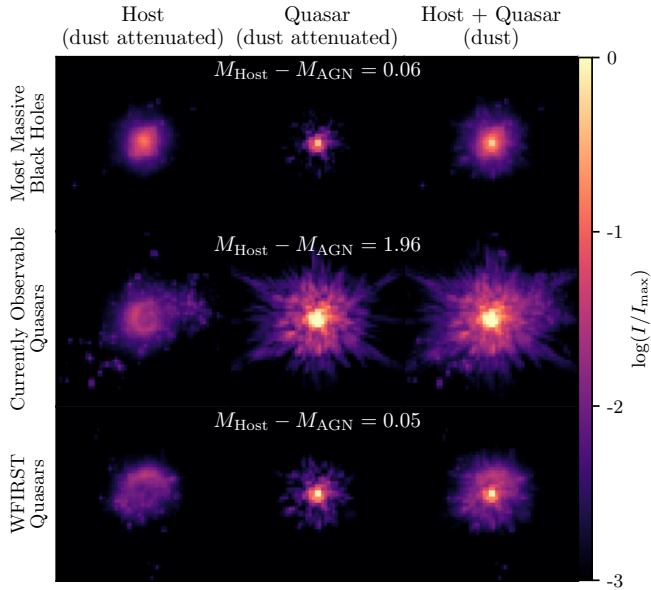


Figure 14. Simulated face-on images of BLUETIDES galaxies in the JWST NIRCam F115W filter, showing the galaxy from each black hole sample that has the lowest contrast ratio between the quasar and the host $M_{\text{UV,Host}(\text{dust})} - M_{\text{UV,AGN}(\text{dust})}$ ($M_{\text{UV,AGN}(\text{dust})} < M_{\text{UV,Host}(\text{dust})}$). The host galaxy emission is shown in the left-most columns, with the emission from the quasar shown in the middle columns. The combined quasar and host galaxy image is shown in the right-most panels. All images include the effect of dust-attenuation. The field-of-view is 10kpc, or $1.86''$. Note that all panels are shown with the same intensity scale.

on the observed black hole–stellar mass relation we make fits to the total sample and the currently observable and WFIRST quasar samples, constraining the slope to be equal to the Kormendy & Ho (2013) best-fitting relation,

$$\log(M_{\text{BH}}/M_{\odot}) = 1.17 \log(M_{*}/M_{\odot}) + b. \quad (7)$$

The Kormendy & Ho (2013) relation has $b = -4.18$. The full BLUETIDES galaxy sample of black holes with $M_{\text{BH}} > 10^{6.5} M_{\odot}$ at $z = 7$ has $b = -4.45$, a 0.27 dex decrease from the Kormendy & Ho (2013) $z = 0$ relation. This decrease in b is not physically significant, as the simulation shows a steeper relation than the observations, and the two relations are reasonably consistent (see Figure 16).

The currently observable quasar sample has a normalization of $b = -4.18$, 0.27 dex higher than that of the full galaxy sample. The WFIRST quasar sample has a normalization of $b = -4.24$, 0.21 dex higher than that of the full sample. Quasar samples are therefore biased samples of the intrinsic black hole–stellar mass relations. This agrees with expectations from observations (e.g. Schulze & Wisotzki 2014; Willott et al. 2017). This simulation provides a calibration of this systematic effect.

6 THE ENVIRONMENTS OF HIGH-REDSHIFT QUASARS

6.1 Distances to the nearest black hole

We now study the environments of high-redshift quasars, by investigating the nearest neighbours to the black hole host galaxies. We

consider the nearest neighbour to be the closest galaxy that hosts a black hole with $M_{\text{BH}} > 10^6 M_{\odot}$. We show the distributions of the distances to these nearest neighbours for the various samples in the top left panel of Figure 17.

We find that the most massive black hole and currently observable quasar samples have closer nearest neighbours than the full black hole sample. We find that 40 per cent of the most massive black holes have their nearest neighbour (with $M_{\text{BH}} > 10^6 M_{\odot}$) within $1R_{\text{vir}}$, compared with 5.9 per cent of currently observable quasars and 21.2 per cent of WFIRST quasars. For comparison, 9.3 per cent of black holes with $M_{\text{BH}} > 10^{6.5} M_{\odot}$ have their nearest neighbour within $1R_{\text{vir}}$.

While the sample size is small, this suggests that the most massive black holes are more likely to be hosted in denser environments than the typical $M_{\text{BH}} > 10^{6.5} M_{\odot}$ black hole, with WFIRST quasars showing a weaker enhancement, and currently observable quasars showing the opposite trend. However, the overall percentage of black holes with nearby neighbours is low and most are instead quite isolated. This indicates that minor mergers play at least some role in growing black holes, but are not necessarily dominant.

We examine one of the most massive black holes which has its nearest neighbour within $1R_{\text{vir}}$ more closely. This black hole has a mass of $\log(M_{\text{BH}}/M_{\odot}) = 8.56$, and is hosted by a galaxy of mass $\log(M_{*}/M_{\odot}) = 11.11$. We find that at $z = 7.0$, its dark matter halo contains 5 additional black holes, with masses $\log(M_{\text{BH}}/M_{\odot}) = (8.20, 7.80, 6.53, 7.06, 5.97)$, in galaxies with stellar masses of $\log(M_{*}/M_{\odot}) = (10.76, 10.83, 9.51, 9.93, 8.89)$. Imaging this system at various redshifts shows that this galaxy has been involved in a recent merger between $z = 7.3$ and $z = 7.0$, with the central black hole (of mass $\log(M_{\text{BH}}/M_{\odot}) = 8.25$ at $z = 7.3$) merging with another black hole of mass $\log(M_{\text{BH}}/M_{\odot}) = 6.37$ (Figure 18).

6.2 Properties of nearby neighbours

We now restrict our investigation to nearest neighbours (with $M_{\text{BH}} > 10^6 M_{\odot}$) which have a distance less than $1R_{\text{vir}}$, and analyse their properties. Figure 17 shows the cumulative distributions of their distance in arcseconds, the UV magnitude of the neighbour, their stellar mass, and the stellar mass ratio of the neighbour to the black hole host.

The most massive black holes, currently observable quasars and WFIRST quasars have a lower proportion of nearby neighbours at distances less than $5''$, relative to the total sample, and their neighbours are brighter. These neighbours (within $1R_{\text{vir}}$) are all brighter than the WFIRST detection limit, and lie within 12 arcseconds of the black hole host, so should be readily detectable by WFIRST or JWST.

The stellar mass distributions of the neighbouring galaxies are consistent between the samples, however as quasars are hosted by massive galaxies, the mass ratios between the neighbour and the black hole host M_{*2}/M_{*1} are significantly lower. More than 70 per cent of these neighbours are less than 1/10th of the stellar mass of the black hole host, and so the majority of these would be classified as only minor mergers. The majority of black hole mass ratios $M_{\text{BH}2}/M_{\text{BH}1}$ are also less than 1/10.

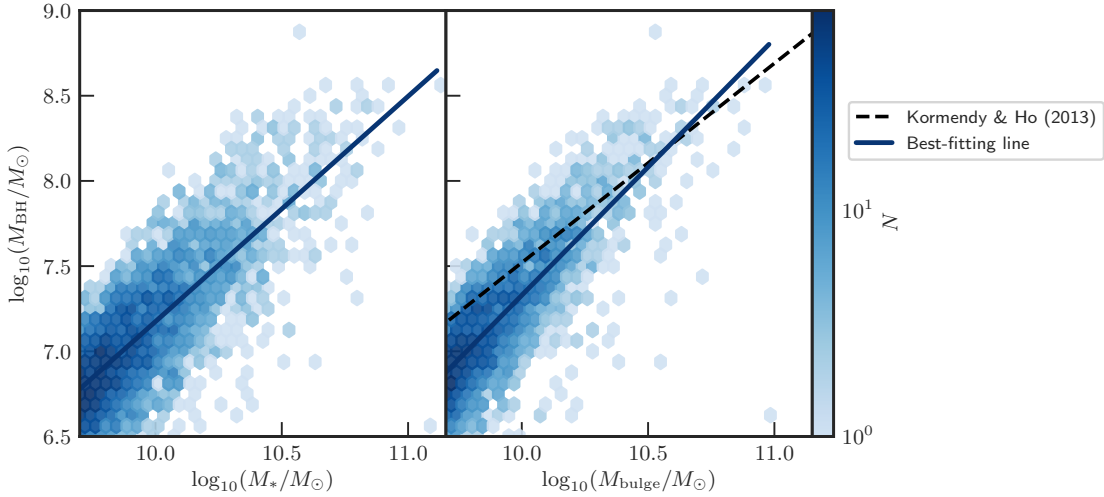


Figure 15. The relation between black hole mass and stellar mass (left) and black hole mass and bulge mass (right) for BLUETIDES galaxies at $z = 7$. Also shown are the best-fitting lines to these relations and the observed relation at $z = 0$ (Kormendy & Ho 2013).

7 CONCLUSIONS

In this paper we use the BLUETIDES simulation to make predictions for the host galaxies of the most massive black holes and quasars at $z = 7$. Our main findings are as follows.

- The 10 most massive black holes are in massive galaxies with stellar masses $\log(M_*/M_\odot) = 10.76^{+0.18}_{-0.16}$, which have a wide range of star formation rates, $50^{+119}_{-35} M_\odot/\text{yr}$. Quasar hosts are less massive, $\log(M_*/M_\odot) = 10.21^{+0.40}_{-0.37}$, with lower star formation rates, $19^{+28}_{-12} M_\odot/\text{yr}$. Lower luminosity quasars host less extreme host galaxies.
- The hosts of the most massive black holes and quasars in BLUETIDES are generally bulge-dominated, with $B/T \simeq 0.85 \pm 0.1$, however their morphologies are not biased relative to the overall $z = 7$ galaxy sample.
- The hosts of the most massive black holes and quasars are compact, with half-mass radii of $R_{0.5} = 0.29^{+0.15}_{-0.10}$ and $0.28^{+0.08}_{-0.06}$ kpc respectively, compared to galaxies of similar mass which have $R_{0.5} = 0.5^{+0.3}_{-0.2}$ kpc.
- Despite its increased resolution over the Hubble Space Telescope, distinguishing the compact host galaxies from the quasar emission will still be challenging with JWST, as shown through our mock images. This will be more successful for those that have the lowest contrast ratio between the host and the AGN (i.e. the brightest host galaxies).
- The $z = 7$ sample has a black hole–stellar mass relation that is steeper than the local Kormendy & Ho (2013) relation, but the two are reasonably consistent, particularly at the highest masses where the observations are most robust.
- Observations of quasars are biased to measure higher black hole–stellar mass relations. The currently observable quasar and WFIRST quasar samples have black hole–stellar mass relations 0.27 and 0.21 dex higher than the total galaxy sample, respectively, providing an estimate of the systematic offset of quasar observations of the $M_* - M_{\text{BH}}$ relation from the true population.
- Black hole hosts are generally isolated, with 40.0 percent of the most massive black holes having neighbours within $1R_{\text{vir}}$, com-

pared to 21.2 per cent of currently observable quasars—more than the average $M_{\text{BH}} > 10^{6.5} M_\odot$ black hole (9.3 per cent). This indicates that minor mergers play an important but not necessarily dominant role in growing black holes.

ACKNOWLEDGEMENTS

This research was supported by the Australian Research Council Centre of Excellence for All Sky Astrophysics in 3 Dimensions (ASTRO 3D), through project number CE170100013. The BLUETIDES simulation was run on the BlueWaters facility at the National Center for Supercomputing Applications. Part of this work was performed on the OzSTAR national facility at Swinburne University of Technology, which is funded by Swinburne University of Technology and the National Collaborative Research Infrastructure Strategy (NCRIS). MAM acknowledges the support of an Australian Government Research Training Program (RTP) Scholarship. TDM acknowledges funding from NSF ACI-1614853, NSF AST-1517593, NSF AST-1616168 and NASA ATP 19-ATP19-0084. TDM and RAC also acknowledge ATP 80NSSC18K101 and NASA ATP 17-0123. This paper makes use of version 17.00 of Cloudy, last described by Ferland et al. (2017).

REFERENCES

- Amiaux J., et al., 2012, in Clampin M. C., Fazio G. G., MacEwen H. A., Oschmann J. M., eds, Space Telescopes and Instrumentation 2012: Optical, Infrared, and Millimeter Wave. SPIE, doi:10.1117/12.926513
- Bañados E., et al., 2016, The Astrophysical Journal Supplement Series, 227, 11
- Bañados E., et al., 2017, arXiv e-prints
- Barth A. J., Martini P., Nelson C. H., Ho L. C., 2003, The Astrophysical Journal Letters, 594, L95
- Battaglia N., Trac H., Cen R., Loeb A., 2013, The Astrophysical Journal, 776, 81
- Bertoldi F., et al., 2003, Astronomy & Astrophysics, 409, L47
- Davies F. B., et al., 2018, The Astrophysical Journal, 864, 142

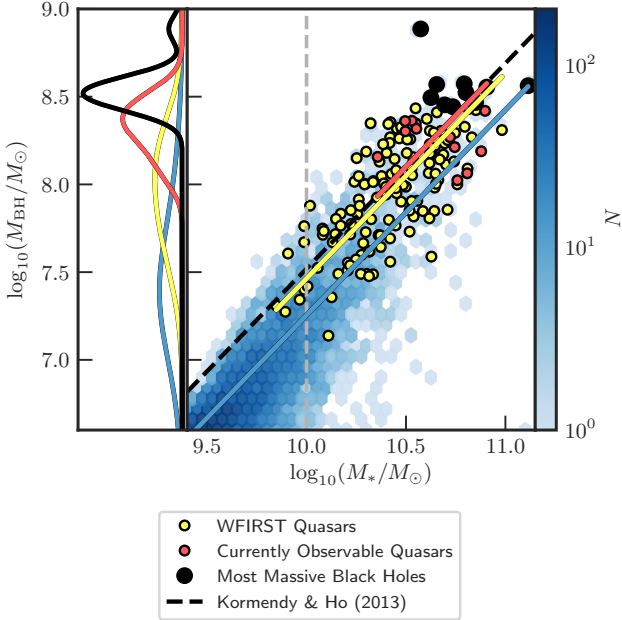


Figure 16. The relation between black hole mass and stellar mass. The blue density plot shows the distribution for all BLUETIDES galaxies, while the circles show the most massive black holes, currently observable quasar and WFIRST quasar samples (see legend). Also plotted is the local observed black hole–mass relation (Kormendy & Ho 2013). The solid lines are fits to the total (blue), currently observable quasar (red) and WFIRST (yellow) samples, constraining the slope to be the same as the Kormendy & Ho (2013) best-fitting relation (Equation 7). The left panel shows the distribution of black hole mass for galaxies with $M_* > 10^{10} M_\odot$, for the total sample (blue line), most massive black holes (black line), currently observable quasars (red line), and WFIRST quasars (yellow line). $M_* = 10^{10} M_\odot$ is shown in the right panel for reference (grey dashed line)

- Davis M., Efstathiou G., Frenk C. S., White S. D. M., 1985, *The Astrophysical Journal*, 292, 371
 DeGraf C., Matteo T. D., Khandai N., Croft R., Lopez J., Springel V., 2012a, *Monthly Notices of the Royal Astronomical Society*, 424, 1892
 DeGraf C., Matteo T. D., Khandai N., Croft R., 2012b, *The Astrophysical Journal*, 755, L8
 DeGraf C., Matteo T. D., Treu T., Feng Y., Woo J.-H., Park D., 2015, *Monthly Notices of the Royal Astronomical Society*, 454, 913
 Di Matteo T., Springel V., Hernquist L., 2005, *Nature*, 433, 604
 Di Matteo T., Khandai N., DeGraf C., Feng Y., Croft R. A. C., Lopez J., Springel V., 2012, *The Astrophysical Journal*, 745, L29
 Di Matteo T., Croft R. A. C., Feng Y., Waters D., Wilkins S., 2017, *Monthly Notices of the Royal Astronomical Society*, 467, 4243
 Fan X., et al., 2000, *The Astronomical Journal*, 120, 1167
 Fan X., et al., 2001, *The Astronomical Journal*, 122, 2833
 Fan X., et al., 2003, *The Astronomical Journal*, 125, 1649
 Fan X., et al., 2004, *The Astronomical Journal*, 128, 515
 Fan X., et al., 2006a, *The Astronomical Journal*, 131, 1203
 Fan X., et al., 2006b, *The Astronomical Journal*, 132, 117
 Fanidakis N., Macciò A. V., Baugh C. M., Lacey C. G., Frenk C. S., 2013, *Monthly Notices of the Royal Astronomical Society*, 436, 315
 Faucher-Giguère C.-A., Lidz A., Zaldarriaga M., Hernquist L., 2009, *The Astrophysical Journal*, 703, 1416
 Feng Y., Matteo T. D., Croft R., Khandai N., 2014, *Monthly Notices of the*

- Royal Astronomical Society, 440, 1865
 Feng Y., Di-Matteo T., Croft R. A., Bird S., Battaglia N., Wilkins S., 2015, *Monthly Notices of the Royal Astronomical Society*, 455, 2778
 Ferland G. J., et al., 2017, *Revista Mexicana de Astronomía y Astrofísica*, 53, 385
 Gardner J. P., et al., 2006, *Space Science Reviews*, 123, 485
 Greig B., Mesinger A., 2017, *Monthly Notices of the Royal Astronomical Society*, 465, 4838
 Greig B., Mesinger A., Bañados E., 2019, *Monthly Notices of the Royal Astronomical Society*, 484, 5094
 Hinshaw G., et al., 2013, *The Astrophysical Journal Supplement Series*, 208, 19
 Huang K.-W., Matteo T. D., Bhowmick A. K., Feng Y., Ma C.-P., 2018, *Monthly Notices of the Royal Astronomical Society*, 478, 5063
 Izumi T., et al., 2018, *Publications of the Astronomical Society of Japan*, 70
 Jiang L., Fan X., Vestergaard M., Kurk J. D., Walter F., Kelly B. C., Strauss M. A., 2007, *The Astronomical Journal*, 134, 1150
 Jiang L., et al., 2016, *The Astrophysical Journal*, 833, 222
 Kashikawa N., et al., 2015, *The Astrophysical Journal*, 798, 28
 Katz N., Hernquist L., Weinberg D. H., 1999, *The Astrophysical Journal*, 523, 463
 Khandai N., Feng Y., DeGraf C., Matteo T. D., Croft R. A. C., 2012, *Monthly Notices of the Royal Astronomical Society*, 423, 2397
 Kormendy J., Ho L. C., 2013, *Annual Review of Astronomy and Astrophysics*, 51, 511
 Krumholz M. R., Gnedin N. Y., 2011, *The Astrophysical Journal*, 729, 36
 Kurk J. D., et al., 2007, *The Astrophysical Journal*, 669, 32
 Lupi A., Volonteri M., Decarli R., Bovino S., Silk J., Bergeron J., 2019, *Monthly Notices of the Royal Astronomical Society*, 488, 4004
 Madau P., 1995, *The Astrophysical Journal*, 441, 18
 Matsuoka Y., et al., 2018a, *Publications of the Astronomical Society of Japan*, 70
 Matsuoka Y., et al., 2018b, *The Astrophysical Journal*, 869, 150
 Mechtley M., et al., 2012, *The Astrophysical Journal*, 756, L38
 Mor R., Netzer H., Trakhtenbrot B., Shemmer O., Lira P., 2012, *The Astrophysical Journal*, 749, L25
 Mortlock D. J., et al., 2011, *Nature*, 474, 616
 Narayanan D., Cox T. J., Hayward C. C., Younger J. D., Hernquist L., 2009, *Monthly Notices of the Royal Astronomical Society*, 400, 1919
 Netzer H., Mor R., Trakhtenbrot B., Shemmer O., Lira P., 2014, *The Astrophysical Journal*, 791, 34
 Ni Y., Matteo T. D., Gilli R., Croft R. A. C., Feng Y., Norman C., , arXiv e-prints, p. arXiv:1912.03780
 Ni Y., Di Matteo T., Feng Y., Croft R. A. C., Tenneti A., 2018, *MNRAS*, 481, 4877
 Okamoto T., Frenk C. S., Jenkins A., Theuns T., 2010, *MNRAS*, 406, 208
 Riechers D. A., Walter F., Carilli C. L., Bertoldi F., 2007, *The Astrophysical Journal Letters*, 671, L13
 Rosa G. D., Decarli R., Walter F., Fan X., Jiang L., Kurk J., Pasquali A., Rix H. W., 2011, *The Astrophysical Journal*, 739, 56
 STScI Development Team 2018, synphot: Synthetic photometry using Astropy, *Astrophysics Source Code Library* (ascl:1811.001), <https://ui.adsabs.harvard.edu/abs/2018ascl.soft11001s>
 Scannapieco C., White S. D. M., Springel V., Tissera P. B., 2009, *MNRAS*, 396, 696
 Schulze A., Wisotzki L., 2014, *Monthly Notices of the Royal Astronomical Society*, 438, 3422
 Shao Y., et al., 2019, *The Astrophysical Journal*, 876, 99
 Shen Y., et al., 2007, *The Astronomical Journal*, 133, 2222
 Shields G. A., Menezes K. L., Massart C. A., Bout P. V., 2006, *The Astrophysical Journal*, 641, 683
 Spergel D., et al., 2015
 Springel V., Hernquist L., 2003, *MNRAS*, 339, 289
 Springel V., Di Matteo T., Hernquist L., 2005a, *MNRAS*, 361, 776
 Springel V., et al., 2005b, *Nature*, 435, 629
 Stanway E. R., Eldridge J. J., 2018, *Monthly Notices of the Royal Astronomical Society*, 479, 75

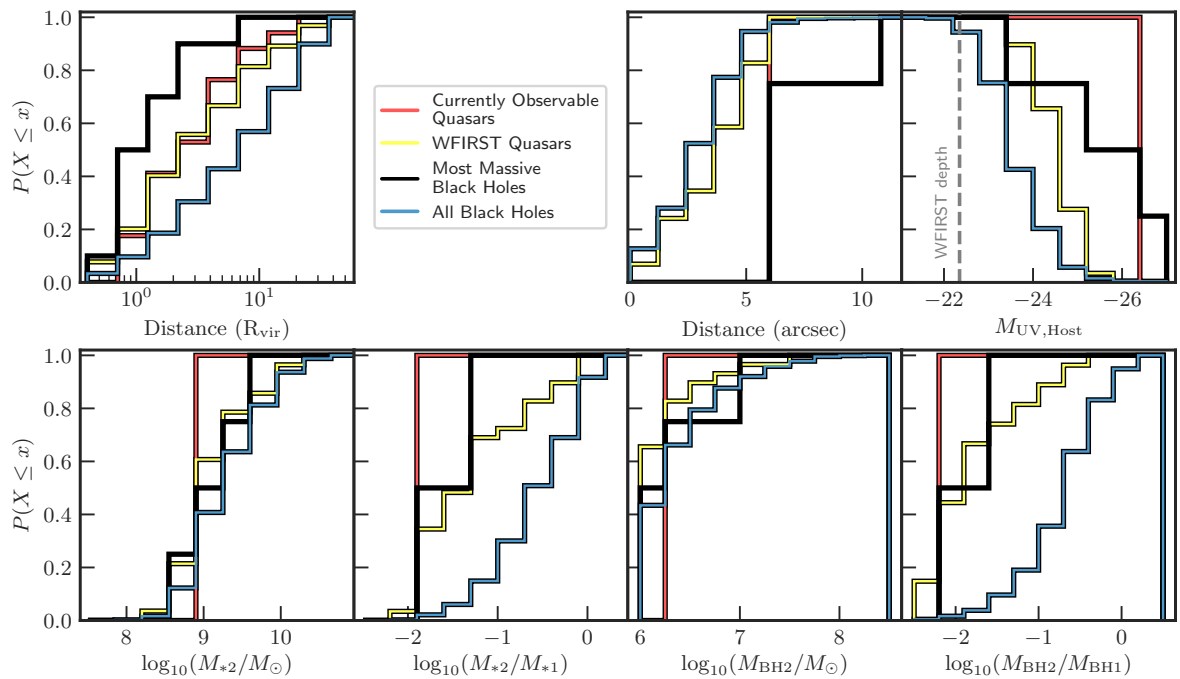


Figure 17. Top left panel: the cumulative distribution of the distance to the nearest $M_{\text{BH}} > 10^6 M_{\odot}$ black hole or ‘nearest neighbour’ for each of the black holes in the various samples (see legend), in terms of the virial radius. Other panels: The properties of the nearest neighbours which have a distance of less than $1R_{\text{vir}}$. The various panels show cumulative distribution functions for the distance to the nearest neighbour in arcseconds, the UV magnitude of the neighbouring galaxy, their stellar mass, and the stellar mass ratio of the neighbour’s mass to that of the sample black hole’s host.

- Tacchella S., et al., 2019, Monthly Notices of the Royal Astronomical Society, 487, 5416
- Tenneti A., Wilkins S. M., Matteo T. D., Croft R. A. C., Feng Y., 2018, Monthly Notices of the Royal Astronomical Society, 483, 1388
- Trakhtenbrot B., Lira P., Netzer H., Cicone C., Maiolino R., Shemmer O., 2018, Frontiers in Astronomy and Space Sciences
- Valiante R., Schneider R., Salvadori S., Gallerani S., 2014, Monthly Notices of the Royal Astronomical Society, 444, 2442
- Venemans B. P., 2017, The Messenger, 169, 48
- Venemans B. P., Walter F., Zschaechner L., Decarli R., Rosa G. D., Findlay J. R., McMahon R. G., Sutherland W. J., 2015, The Astrophysical Journal, 816, 37
- Venemans B. P., Neeleman M., Walter F., Novak M., Decarli R., Hennawi J. F., Rix H.-W., 2019, The Astrophysical Journal, 874, L30
- Vogelsberger M., Genel S., Sijacki D., Torrey P., Springel V., Hernquist L., 2013, MNRAS, 436, 3031
- Vogelsberger M., et al., 2014, MNRAS, 444, 1518
- Volonteri M., 2012, Science, 337, 544
- Walter F., et al., 2003, Nature, 424, 406
- Walter F., Carilli C., Bertoldi F., Menten K., Cox P., Lo K. Y., Fan X., Strauss M. A., 2004, The Astrophysical Journal, 615, L17
- Wang R., et al., 2010, The Astrophysical Journal, 714, 699
- Wang R., et al., 2011, The Astronomical Journal, 142, 101
- Wang R., et al., 2013, The Astrophysical Journal, 773, 44
- Wang F., et al., 2018, arXiv e-prints, p. arXiv:1810.11926
- Waters D., Matteo T. D., Feng Y., Wilkins S. M., Croft R. A. C., 2016, Monthly Notices of the Royal Astronomical Society, 463, 3520
- Wilkins S. M., Feng Y., Matteo T. D., Croft R., Lovell C. C., Waters D., 2017, Monthly Notices of the Royal Astronomical Society, 469, 2517
- Willott C. J., et al., 2010a, The Astronomical Journal, 139, 906
- Willott C. J., et al., 2010b, The Astronomical Journal, 140, 546
- Willott C. J., Bergeron J., Omont A., 2017, The Astrophysical Journal, 850, 108

This paper has been typeset from a $\text{\TeX}/\text{\LaTeX}$ file prepared by the author.

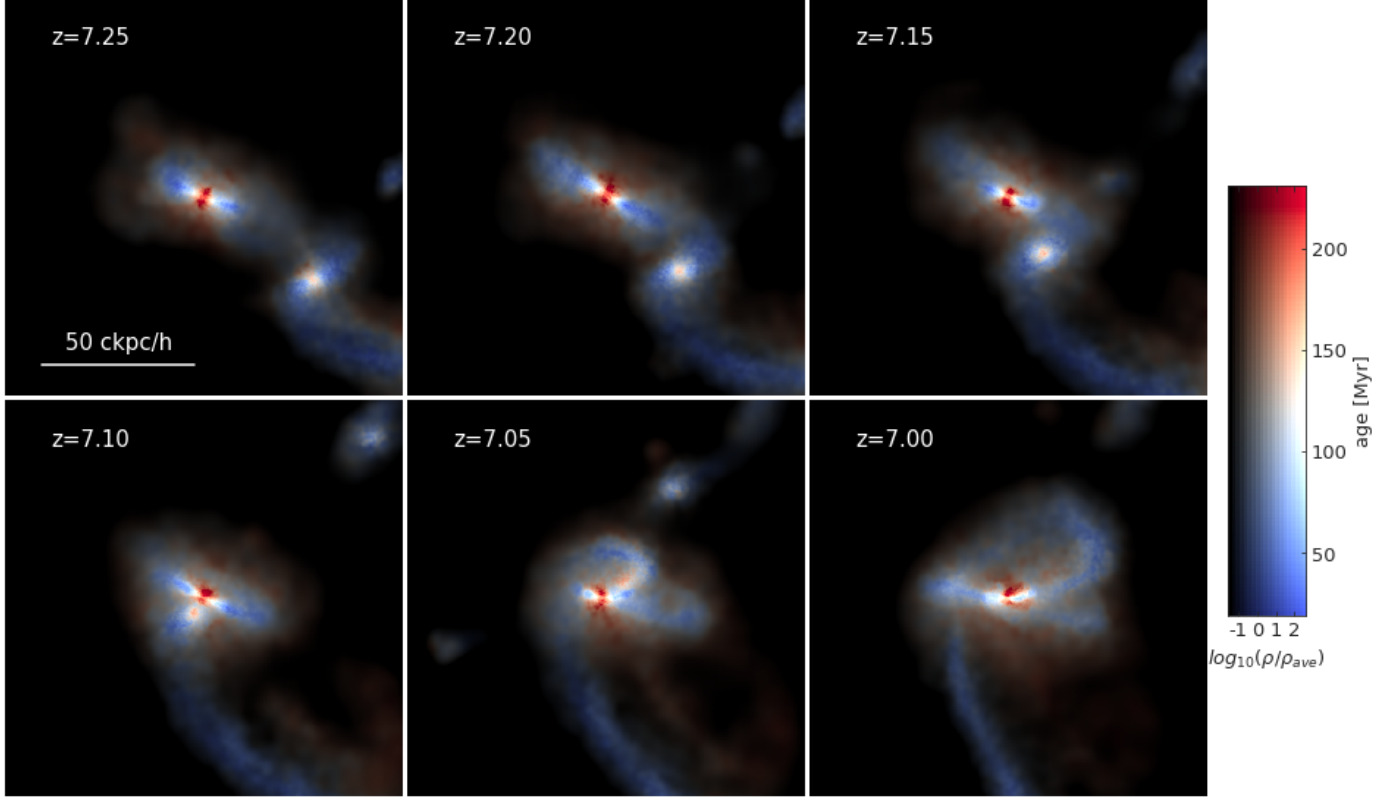


Figure 18. The host galaxies of two merging black holes from $z = 7.25$ to $z = 7.0$. At $z = 7.3$, the primary black hole (at the centre of the images) has a black hole mass of $\log(M_{\text{BH}}/M_{\odot}) = 8.25$, while the companion has a mass of $\log(M_{\text{BH}}/M_{\odot}) = 6.37$ and is at a distance of 82 ckpc or 9.9 kpc from the primary black hole. The black hole which results from this merger is one of the ten most massive black holes in the simulation at $z = 7$, with a mass of $\log(M_{\text{BH}}/M_{\odot}) = 8.56$, in a galaxy with a stellar mass of $\log(M_{*}/M_{\odot}) = 11.11$. Each panel is $120/h$ ckpc per side, showing the stellar density color coded by the age of star (from blue to red indicating young to old populations respectively).